Journal of Computational Physics 228 (2009) 2063–2081

Contents lists available at ScienceDirect

Journal of Computational Physics

journal homepage: www.elsevier.com/locate/jcp

Stochastic modeling of evaporating sprays within a consistent hybrid joint PDF framework

Gaurav Anand *, Patrick Jenny

Institute of Fluid Dynamics, Sonneggstrasse 3, ETH Zurich, Zuerich CH-8092, Switzerland

ARTICLE INFO

Article history:
Received 26 August 2008
Received in revised form 20 November 2008
Accepted 21 November 2008
Available online 6 December 2008

Keywords:
PDF method
Stochastic method
Spray
Evaporation
Multi-phase flow
Turbulent flow
Hybrid algorithm
Particle local time-stepping
Time-averaging

ABSTRACT

In the present study, a framework for modeling two-phase evaporating flow is presented, which employs an Eulerian–Lagrangian–Lagrangian approach. For the continuous phase, a joint velocity-composition probability density function (PDF) method is used. Opposed to other approaches, such PDF methods require no modeling for turbulent convection and chemical source terms. For the dispersed phase, the PDF of velocity, diameter, temperature, seen gas velocity and seen gas composition is calculated. This provides a unified formulation, which allows to consistently address the different modeling issues associated with such a system. Because of the high dimensionality, particle methods are employed to solve the PDF transport equations. To further enhance computational efficiency, a local particle time-stepping algorithm is implemented and a particle time-averaging technique is employed to reduce statistical and bias errors. In comparison to previous studies, a significantly smaller number of droplet particles per grid cell can be employed for the computations, which rely on two-way coupling between the droplet and gas phases. The framework was validated using established experimental data and a good overall agreement can be observed.

1. Introduction

Two-phase flow is a highly complex problem characterised by strong non-linear coupling, like gas turbulence influencing droplet motion and evaporation, and vice versa. Combustion of the formed charge, i.e. mixture of vapourised droplets and air, further complicates the problem. An accurate prediction of such a flow requires accurate description of both the continuous and the dispersed phases. A vast literature is available on the various modeling approaches used to simulate such two-phase flow systems. Loth [1] reviewed the numerical developments in this field and categorised them as Lagrangian–Lagrangian, Eulerian–Eulerian and Eulerian–Lagrangian approaches, depending on the representation of the continuous and the dispersed phases, respectively. Rangel [2] used a Lagrangian–Lagrangian approach for the gas and dispersed phase momentum equations, and an Eulerian scheme for the fuel-vapour continuity and energy equations. However, the work lacks in consistently addressing the issues associated with the exchange of information between the Lagrangian and Eulerian flow descriptions. In another work [3], an Eulerian–Eulerian approach was employed to simulate dense sprays, where the dispersed phase is treated as a continuum embedded within the gas phase [3]. This helps to avoid the need to directly resolve the particle–particle interactions.

In the present study, we restrict ourselves to the dilute spray regime, where the dispersed phase cannot be treated as a continuum and the particle–particle interactions can be neglected. The Eulerian–Lagrangian approach [3–7] is quite popular and has been successful for many spray combustion simulations. In such a method, the gas and the dispersed phases are

* Corresponding author.
E-mail addresses: anand@ifd.mavt.ethz.ch, anand@cantab.net (G. Anand), jenny@ifd.mavt.ethz.ch (P. Jenny).

0021-9991/$ - see front matter © 2008 Elsevier Inc. All rights reserved.
doi:10.1016/j.jcp.2008.11.022

treated by an Eulerian (finite-volume) and a Lagrangian framework, respectively and Loth [1] argues that it is helpful to reduce coupling errors. However, a discussion on evaporating spray simulations is missing in his review.

Here, a new framework capable of simulating turbulent reactive evaporating sprays is presented. It is based on an Eulerian–Lagrangian–Lagrangian approach; similar to the one presented by Naud [8]. For the mean gas phase flow, a finite-volume (Eulerian) scheme is employed to solve the Reynolds averaged Navier–Stokes (RANS) equations and to obtain the higher statistical moments, a particle method (Lagrangian) is used to solve the joint velocity–frequency-composition probability density function (PDF) transport equation as presented by Jenny et al. [9]. They showed that such PDF solution algorithms for turbulent reactive flows are computationally very efficient [9]. A particle method (Lagrangian) is also used for the dispersed phase. It is shown how the two phases can be rigorously coupled and for the droplet dispersion a novel model is presented. It is also demonstrated that the bias error and therefore the required number of particles can be drastically reduced by exponentially weighted moving time-averaging [9]. Moreover, a local time-stepping algorithm for the particles has been implemented to enhance numerical efficiency [10]. To model the droplet evaporation, a model based on Sazhin et al. [11] is employed. A brief validation study shows excellent agreement with the experimental microgravity data of Nomura et al. [12]. For the validation of the whole framework, the well established experimental data of Sommerfeld et al. [13] for evaporating iso-propyl alcohol droplets was employed.

2. Statistical description of the continuous phase

In this section, a statistical description of the continuous phase flow is presented. It is based on an Eulerian and a discrete Lagrangian approach, where the state of the flow is described by a joint probability density function (PDF). For simplicity, in this work no chemical reactions nor mixing are considered.

2.1. Mass density function

The one-point one-time statistics of the continuous phase flow is characterised by the mean gas density $\langle\rho\rangle$, the Favre (or mass) averaged velocity $\widetilde{\mathbf{U}}$ and by the mass weighted Eulerian PDF $\tilde{f}(\mathbf{v},\boldsymbol{\Psi};\mathbf{x},t)$ of fluctuating velocity $\mathbf{u}=\mathbf{U}-\widetilde{\mathbf{U}}$ and composition $\boldsymbol{\phi}$ at any location $\mathbf{x}$, and time t [9,14,15]. Note that $\mathbf{v}$ and $\boldsymbol{\Psi}$ are the sample space variables of $\mathbf{u}$ and $\boldsymbol{\phi}$, respectively. Transport of the mass density function (MDF) $\mathcal{F}(\mathbf{v},\boldsymbol{\Psi},\mathbf{x},t)=\langle\rho\rangle(\mathbf{x},t)\tilde{f}(\mathbf{v},\boldsymbol{\Psi};\mathbf{x},t)$ is described by

$$\begin{aligned}&\frac{\partial\mathcal{F}}{\partial t}+\frac{\partial\mathcal{F}(\widetilde{U}_j+v_j)}{\partial x_j}-\frac{\partial\widetilde{U}_i}{\partial x_j}\frac{\partial\mathcal{F}v_j}{\partial v_i}+\frac{1}{\langle\rho\rangle}\frac{\partial\langle\rho\rangle\widetilde{u_iu_j}}{\partial x_j}\frac{\partial\mathcal{F}}{\partial v_i}+\frac{\partial\mathcal{F}S_\alpha}{\partial\psi_\alpha}-\frac{1}{\langle\rho\rangle}\frac{\partial\langle J_i^\alpha\rangle}{\partial x_i}\frac{\partial\mathcal{F}}{\partial\psi_\alpha}\\&\quad=\frac{\partial}{\partial v_i}\left(\mathcal{F}\left\langle\frac{1}{\rho}\frac{\partial p}{\partial x_i}-\frac{1}{\langle\rho\rangle}\frac{\partial\langle p\rangle}{\partial x_i}-\frac{1}{\rho}\frac{\partial\tau_{ij}}{\partial x_j}+\frac{1}{\langle\rho\rangle}\frac{\partial\langle\tau_{ij}\rangle}{\partial x_j}\middle|\mathbf{v},\boldsymbol{\Psi}\right\rangle\right)+\frac{\partial}{\partial\psi_\alpha}\left(\mathcal{F}\left\langle\frac{1}{\rho}\frac{\partial J_i^\alpha}{\partial x_i}-\frac{1}{\langle\rho\rangle}\frac{\partial\langle J_i^\alpha\rangle}{\partial x_i}\middle|\mathbf{v},\boldsymbol{\Psi}\right\rangle\right)+S_{\text{droplet}},\end{aligned}\tag{1}$$

where the operators $\tilde{\cdot}$, $\langle\cdot\rangle$ and $\langle\cdot|\cdot\rangle$ denote Favre-averaged quantities, Reynolds-averaged quantities, and conditional expectations respectively. The first and second terms on the left-hand side (LHS) describe the temporal evolution and transport in physical space. The third and fourth LHS-terms represent the evolution of $\mathcal{F}$ in the fluctuating velocity space due to the mean velocity and Reynolds stress gradients. The last two LHS-terms describe the evolution of $\mathcal{F}$ in the composition space due to chemical reactions and mean diffusion. Note that all LHS-terms appear in closed form. Those on the right-hand side (RHS), however, are unclosed and require modeling. They account for the effects of the fluctuating pressure gradient term, the fluctuating viscous term and the fluctuating diffusion term.

Since $\mathcal{F}$ is transported in $6+N_s$ dimensions (N_s is the number of compositions), it generally is infeasible to solve Eq. (1) with a finite-volume, a finite-difference or any other continuum method. Fortunately, the cost of stochastic Monte-Carlo methods scales only linearly with the sample space dimension. In such methods, $\mathcal{F}$ is represented by a cloud of particles. For each particle, a set of stochastic differential equations has to be solved to describe its evolution.

2.2. RANS formulation

Jenny and Pope [9] showed the relationship between the joint velocity-composition PDF equation and the Reynolds averaged Navier–Stokes (RANS) equations. The RANS equations can directly be derived from Eq. (1) and if all viscous and diffusive terms are neglected (which is justified for high Reynolds numbers away from walls), the system reads

$$\frac{\partial}{\partial t}\langle\rho\rangle+\frac{\partial}{\partial x_i}(\langle\rho\rangle\widetilde{U}_i)=\langle S_m^I\rangle,\tag{2}$$

$$\frac{\partial}{\partial t}(\langle\rho\rangle\widetilde{U}_i)+\frac{\partial}{\partial x_j}(\langle\rho\rangle\widetilde{U}_i\widetilde{U}_j+\langle p\rangle\delta_{ij})=-\frac{\partial}{\partial x_j}(\langle\rho\rangle\widetilde{u_iu_j})+\langle S_{U_i}^I\rangle,\tag{3}$$

$$\begin{aligned}&\frac{\partial}{\partial t}(\langle\rho\rangle\widetilde{E}_s)+\frac{\partial}{\partial x_i}(\langle\rho\rangle\widetilde{U}_i(\widetilde{E}_s+\langle p\rangle))\\&\quad=\langle\rho\dot{Q}\rangle-\frac{\partial}{\partial x_i}(\langle\rho\rangle\widetilde{u_ih_s''})-\frac{\partial}{\partial x_i}\left(\frac{\langle\rho\rangle}{2}\widetilde{u_iu_ju_j}\right)-\frac{\partial}{\partial x_i}(\widetilde{U}_j\langle\rho\rangle\widetilde{u_iu_j})+\langle S_H^I\rangle,\end{aligned}\tag{4}$$

where E_s is the total sensible energy, h_s the sensible enthalpy and $\dot{Q}$ the thermal energy source term due to chemical reactions. Note that $\widetilde{u_i u_j}$, $\widetilde{u_i h_s''}$, $\widetilde{u_i u_j u_j}$ and $\langle \rho \dot{Q} \rangle$ can be obtained from $\mathcal{F}$. Therefore, opposed to moment closure methods, such a PDF approach requires no modeling for turbulent convection and chemical source terms (arising due to chemical reactions).

In the present study we propose a framework for modeling two-phase reacting flow. The term $\langle S_m^l \rangle$ in Eq. (2) is the mean mass transfer source term arising due to droplet evaporation and the term $\langle S_{U_i}^l \rangle$ in Eq. (3) is the mean momentum source term arising due to the droplet motion in the gas environment. $\langle S_H^l \rangle$ in Eq. (4) accounts for the energy consumed during droplet heating and evaporation, which for dilute sprays is much less than the energy released during combustion, i.e. $\langle \rho \dot{Q} \rangle \gg \langle S_H^l \rangle$. Thus, $\langle S_H^l \rangle$ in Eq. (4) is neglected. Expressions for the expectations $\langle S_m^l \rangle$ and $\langle S_{U_i}^l \rangle$ will be presented in Section (3.4).

2.3. PDF closure models for the continuous phase

The relationship between the mass weighted PDF $\tilde{f}$ and the MDF $\mathcal{F}$ is given as,

$$\langle \rho \rangle \tilde{f}(\mathbf{v}, \mathbf{\Psi}, \Theta; \mathbf{x}, t) = \mathcal{F}(\mathbf{v}, \mathbf{\Psi}, \Theta, \mathbf{x}, t) \equiv \rho(\mathbf{\Psi}) \langle \delta(\mathbf{u} - \mathbf{v}) \delta(\boldsymbol{\phi} - \mathbf{\Psi}) \delta(\omega - \Theta) \delta(\mathbf{X} - \mathbf{x}) \rangle, \tag{5}$$

where the sample space was augmented by the coordinate Θ for the turbulent frequency ω. According to Eq. (5), $\mathcal{F}$ can be represented by a cloud of particles in which it expresses the local particle number density.

In the present study, we use the hybrid particle/finite-volume approach [9] to solve Eqs. (1)–(4). In this approach, Eq. (1) is solved with a particle method, where closure models are employed for the RHS terms and $\widetilde{\mathbf{U}}$ is obtained from the solution of the system ((2)–(4)), which is solved simultaneously with a FV scheme. Note that $\widetilde{u_i u_j}$, $\widetilde{u_i h_s''}$, $\widetilde{u_i u_j u_j}$ and $\langle \rho \dot{Q} \rangle$ are obtained from the particle solution of Eq. (1) and the mean pressure is given by the state equation

$$\langle p \rangle = \langle (\gamma - 1)(\rho E - \frac{\rho}{2} U_i U_i) \rangle, \tag{6}$$

where γ is the ratio of specific heats. The specific heat constants of the gas are assumed to be constant. While a standard upwind based second order, explicit FV scheme is employed to solve the RANS equations, the particle method used to compute $\mathcal{F}$ is more involved and is explained in more detail here.

Each particle has a mass m^*, a position $\mathbf{X}^*$, a fluctuating velocity $\mathbf{u}^*$, a turbulence frequency ω^* and a set of compositions $\boldsymbol{\phi}^*$. Their evolution in physical space is described by the equation

$$d\mathbf{X}^* = (\widetilde{\mathbf{U}}(\mathbf{X}^*) + \mathbf{u}^*) dt, \tag{7}$$

where the mean velocity $\widetilde{\mathbf{U}}$ is obtained from the RANS solution and interpolated to the particle positions. The evolution

$$\frac{du_i^*}{dt} = \frac{1}{\langle \rho \rangle} \frac{\partial \langle \rho \rangle \widetilde{u_i u_j}}{\partial x_j} - u_j^* \frac{\partial \widetilde{U}_i}{\partial x_j} - \frac{1}{\rho} \frac{\partial p}{\partial x_i} + \frac{1}{\rho} \frac{\partial \tau_{ij}}{\partial x_j} + \frac{1}{\langle \rho \rangle} \frac{\partial \langle p \rangle}{\partial x_i} - \frac{1}{\langle \rho \rangle} \frac{\langle \partial \tau_{ij} \rangle}{\partial x_j} \tag{8}$$

of the fluctuating particle velocity is approximated by the Simplified Langevin Model (SLM), i.e. as

$$du_i^*(t) = \frac{1}{\langle \rho \rangle} \frac{\delta \langle \rho \rangle \widetilde{u_i u_j}}{\delta x_j} dt - u_j^* \frac{\delta \widetilde{U}_i}{\delta x_j} dt - \left(\frac{1}{2} + \frac{3}{4} C_0 \right) \Omega u_i^* dt + (C_0 k \Omega)^{1/2} dW_i, \tag{9}$$

where

$$k = \frac{1}{2} \widetilde{u_i u_i} \tag{10}$$

is the mean turbulent kinetic energy and

$$\Omega \equiv C_\Omega \widetilde{\omega | \omega \geqslant \tilde{\omega}} \tag{11}$$

Table 1
Model constants.

Constant	Value	Used in
C_0	2.1	SLM
C_Ω	0.6893	Definition of Ω
$C_{\omega 1}$	0.7	Turbulence frequency model
C_{ω_2}	0.9	Turbulence frequency model
C_3	1.0	Turbulence frequency model
C_4	0.25	Turbulence frequency model

the conditional turbulence frequency. Typical values for the model constants C_0 and C_Ω are given in Table 1. The last term in Eq. (9) is based on a Wiener process, where $dW_i(t) = W_i(t+dt) - W_i(t)$ is a Gaussian random variable with $\langle dW_i \rangle \equiv 0$ and $\langle dW_i dW_j \rangle = dt\delta_{ij}$. To describe the evolution of the turbulence frequency ω^*, the model equation

$$d\omega^*(t) = -C_3(\omega^* - \tilde{\omega})\Omega dt - S_\omega \Omega \omega^*(t)dt + (2C_3C_4\tilde{\omega}\Omega\omega^*(t))^{1/2}dW \tag{12}$$

with the source term

$$S_\omega = C_{\omega 2} - C_{\omega 1}\frac{P}{k\Omega} \tag{13}$$

and the turbulence production

$$P = -\widetilde{u_i u_j}\frac{\partial \tilde{U}_i}{\partial x_j} \tag{14}$$

is employed. Again, typical values for the model constants C_3, C_4, $C_{\omega 1}$ and $C_{\omega 2}$ are specified in Table 1. Details regarding the numerical solution of Eqs. (9), (11) and (12) can be found in [9].

3. Statistical description of the dispersed phase

Similar to the gas phase, in this section a statistical description of the dispersed phase flow is presented. In the present study, all droplets are assumed to be spherical and have constant density throughout the flow.

3.1. Mass density function

To describe the statistics of the spray droplet distribution, here the mass density function

$$\mathcal{F}_p(\mathbf{V}_p, \widehat{D}_p, \mathbf{\Psi}_p, \mathbf{V}_s, \mathbf{\Psi}_s, \mathbf{x}, t) = \langle R \rangle(\mathbf{x}, t)\tilde{f}_p(\mathbf{V}_p, \widehat{D}_p, \mathbf{\Psi}_p, \mathbf{V}_s, \mathbf{\Psi}_s; \mathbf{x}, t)$$

is considered. $\langle R \rangle$ is the average droplet mass density and $\tilde{f}_p$ the mass weighted PDF of the droplet velocity $\mathbf{U}_p$, the droplet diameter D_p, the droplet composition $\mathbf{\Phi}_p$, the "seen" gas velocity $\mathbf{U}_s$, and the "seen" gas composition $\mathbf{\Phi}_s$ at the location $\mathbf{x}$ and time t. Note that $\mathbf{V}_p, \widehat{D}_p, \mathbf{\Psi}_p, \mathbf{V}_s$ and $\mathbf{\Psi}_s$ are the sample space variables of $\mathbf{U}_p, D_p, \mathbf{\Phi}_p, \mathbf{U}_s$ and $\mathbf{\Phi}_s$, respectively. This mass density function provides a unified formulation [8], which allows to consistently address the different modeling issues associated with such a system. The droplet MDF transport equation without droplet coalescence or break-up reads

$$\begin{aligned}\frac{\partial \mathcal{F}_p}{\partial t} + V_{p,j}\frac{\partial \mathcal{F}_p}{\partial x_j} = &-\frac{\partial}{\partial V_{p,i}}\left[\left\langle \frac{DU_{p,i}}{Dt}\middle| \mathbf{V}_p, \widehat{D}_p, \mathbf{\Psi}_p, \mathbf{V}_s, \mathbf{\Psi}_s; \mathbf{x}, t\right\rangle_p \mathcal{F}_p\right] - \frac{\partial}{\partial \widehat{D}_p}\left[\left\langle \frac{DD_p}{Dt}\middle| \mathbf{V}_p, \widehat{D}_p, \mathbf{\Psi}_p, \mathbf{V}_s, \mathbf{\Psi}_s; \mathbf{x}, t\right\rangle_p \mathcal{F}_p\right] \\ &- \frac{\partial}{\partial \Psi_{p,\alpha}}\left[\left\langle \frac{D\Phi_{p,\alpha}}{Dt}\middle| \mathbf{V}_p, \widehat{D}_p, \mathbf{\Psi}_p, \mathbf{V}_s, \mathbf{\Psi}_s; \mathbf{x}, t\right\rangle_p \mathcal{F}_p\right] - \frac{\partial}{\partial V_{s,i}}\left[\left\langle \frac{DU_{s,i}}{Dt}\middle| \mathbf{V}_p, \widehat{D}_p, \mathbf{\Psi}_p, \mathbf{V}_s, \mathbf{\Psi}_s; \mathbf{x}, t\right\rangle_p \mathcal{F}_p\right] \\ &- \frac{\partial}{\partial \Psi_{s,\alpha}}\left[\left\langle \frac{D\Phi_{s,\alpha}}{Dt}\middle| \mathbf{V}_p, \widehat{D}_p, \mathbf{\Psi}_p, \mathbf{V}_s, \mathbf{\Psi}_s; \mathbf{x}, t\right\rangle_p \mathcal{F}_p\right] + \left\langle \frac{1}{m_p}\frac{dm_p}{dt}\middle| \mathbf{V}_p, \widehat{D}_p, \mathbf{\Psi}_p, \mathbf{V}_s, \mathbf{\Psi}_s; \mathbf{x}, t\right\rangle_p \mathcal{F}_p,\end{aligned} \tag{15}$$

where the operator $\langle \cdot \mid \cdot \rangle_p$ denotes conditional expectations of droplet properties. In this paper, d/dt denotes the rate of change of particle properties, while $D/Dt(\partial/\partial t + \boldsymbol{U}\cdot\nabla)$ denotes the substantial derivative. If the particle velocity and $\mathbf{U}$ are identical, then the meaning of the operators becomes the same. Note that the mass of a spherical droplet of diameter D_p is $m_p = \frac{4}{3}\pi D_p^3 \rho_p$.

3.2. Dispersed phase modeling

To solve Eq. (15), a stochastic particle approach similar to the one used for the gas phase turbulence is employed. The dispersed phase is represented by a large set of particles with the individual properties $\mathbb{W}^*$, $\mathbf{X}^*$, $\mathbf{U}_p^*$, D_p^*, $\mathbf{\Phi}_p^*$, $\mathbf{U}_s^*$ and $\mathbf{\Phi}_s^*$, which represent their weight, location in physical space, velocity, droplet diameter, droplet composition, "seen" gas velocity, and "seen" gas composition. Note that such a computational particle represents $n = \mathbb{W}^*/m_p(D_p^*)$ droplet particles.

The motion of the computational particles is governed by the velocity modeled as

$$\frac{dU_{p,i}^*}{dt} = g_i - \frac{1}{\rho_p}\left[\frac{\partial p}{\partial x_i}\right]_s + \frac{U_{s,i}^* - U_{p,i}^*}{\tau_p}, \tag{16}$$

where τ_p is the droplet relaxation time, i.e. $1/\tau_p$ is the rate at which the particle velocity $\mathbf{U}_p$ relaxes to the surrounding ("seen") gas velocity $\mathbf{U}_s$.

The droplet Reynolds number is defined as

$$Re_p = \frac{\rho_g |\mathbf{U}_s - \mathbf{U}_p| D_p}{\mu_g},$$

where μ_g is the viscosity of the surrounding gas. In the Stokes regime ($Re_p \to 0$), the analytically determined particle relaxation time (for a sphere) is

$$\tau_p^{st} = \frac{\rho_p D_p^2}{18\mu_g}. \tag{17}$$

For higher Reynolds numbers, the solution

$$\frac{1}{\tau_p} = \frac{f_1}{\tau_p^{st}}$$

with the Schiller–Naumann correlation [8,16]

$$f_1 = \begin{cases} 1 + 0.15 Re_p^{0.687} & \text{for } Re_p \leqslant 1000 \\ 0.44 \frac{Re_p}{24} & \text{for } Re_p > 1000 \end{cases}$$

is employed. To model the fluctuating "seen" gas velocity $\mathbf{u}_s^* = \mathbf{U}_s^* - \widetilde{\mathbf{U}}(\mathbf{X})^*$ associated with a computational dispersed phase particle, a similar model as for the gas phase particle velocities is used, i.e.

$$\begin{aligned} \frac{du_{s,i}^*}{dt} &= \frac{\partial u_{s,i}^*}{\partial t} + U_{p,j}^* \frac{\partial u_{s,i}^*}{\partial x_j} = \frac{\partial u_{s,i}^*}{\partial t} + (\widetilde{U}_j(\mathbf{X}^*) + u_{s,j}^*) \frac{\partial u_{s,i}^*}{\partial x_j} + (U_{p,j}^* - \widetilde{U}_j(\mathbf{X}^*) - u_{s,j}^*) \frac{\partial u_{s,i}^*}{\partial x_j} \\ &= \frac{1}{\langle\rho\rangle} \frac{\partial}{\partial x_j} (\langle\rho\rangle \widetilde{u_{s,i} u_{s,j}}) - u_{s,j}^* \frac{\partial \widetilde{U}_i}{\partial x_j} - \left(\frac{1}{2} + \frac{3}{4} C_0\right) \Omega u_{s,i}^* + \sqrt{C_0 k \Omega} \frac{dW_i}{dt} + \underbrace{\left(U_{p,j}^* - \widetilde{U}_j(\mathbf{X}^*) - u_{s,j}^*\right) \frac{\partial u_{s,i}^*}{\partial x_j}}_{(I)}. \end{aligned} \tag{18}$$

The term (I) in Eq. (18) accounts for the difference between the trajectories of dispersed and gas phase particles. Since it depends on the instantaneous gradient $\partial u_{s,i}/\partial x_j$ of the fluctuating seen gas velocity, modeling is required. Here, we present a closure for term (I), which is based on the correlation length scale

$$L_{\text{corr}} = \frac{\sqrt{k}}{\Omega}. \tag{19}$$

This lets us formulate the decorrelation model

$$\frac{du_{s,i}^*}{dt} = \frac{1}{\langle\rho\rangle} \frac{\partial}{\partial x_j} (\langle\rho\rangle \widetilde{u_{s,i} u_{s,j}}) - u_{s,j}^* \frac{\partial \widetilde{U}_i}{\partial x_j} - \left(\frac{1}{2} + \frac{3}{4} C_0\right) \Omega u_{s,i}^* + \sqrt{C_0 k \Omega} \frac{dW_i}{dt} - \alpha\, u_{s,i}^* + \sqrt{\frac{4}{3} \alpha k} \frac{dW_i}{dt}, \tag{20}$$

where the decorrelation frequency

$$\alpha = \frac{|\widetilde{\mathbf{U}} + \mathbf{u}_s^* - \mathbf{U}_p^*|}{L_{\text{corr}}} \tag{21}$$

depends on the magnitude of the velocity difference $|\widetilde{\mathbf{U}} + \mathbf{u}_s^* - \mathbf{U}_p^*|$ and the correlation length L_{corr}. In the implementation, the last two terms in Eq. (20) are treated in a fractional step by changing $\mathbf{u}_{s,i}^*$ (computed without the last two terms in Eq. (20)) by the amount

$$\Delta \mathbf{u}_s^{*decorrelation} = (e^{-\alpha \Delta t} - 1)\ \mathbf{u}_s^{*uncorrected} + \sqrt{1 - e^{-2\alpha\Delta t}} \mathbf{u}_g^{random} \tag{22}$$

where the random variable $\mathbf{u}_g^{random}$ is the fluctuating velocity of an arbitrary gas phase particle belonging to the same ensemble. The effect of term (I) on $\mathbf{u}_s^*$ is weak, if the seen gas evolves with a similar velocity as the droplets ($\alpha\Delta t \ll 1$). Vice versa, if droplet and seen gas velocities differ a lot ($\alpha\Delta t \gg 1$), $\mathbf{u}_s^*$ becomes an uncorrelated random variable fulfilling the local gas velocity statistics. Note that the decorrelation scheme preserves the variance of u_s^*, if u_g has the same variance independent of u_s.

3.3. Evaporation sub-model and its validation

Here, an infinite thermal conductivity (ITC) model [17], where one assumes uniform temperature within a droplet, is considered. The heat balance equation for a droplet is given as

$$m_p C_{pL} \frac{dT_p}{dt} = \pi D_p Nu\ k_m (T_g - T_p) - \dot{m}_p L, \tag{23}$$

where $\dot{m}_p$ is the droplet evaporation rate, C_{pL} the specific heat capacity of the liquid droplets, k_m the thermal conductivity of the gas film mixture, T_g the gas temperature, T_p the droplet temperature and L the latent heat of vapourisation. The D^2-law by Spalding [18] is used for the mass evaporation rate, which is given as

$$\dot{m}_p = \pi D_p \rho_m\ D_v\ Sh\ \ln(1 + B_M), \tag{24}$$

where D_v is the binary diffusivity. The Spalding mass transfer number is given as

$$B_M = \frac{Y_m - Y_\infty}{1 - Y_m},$$

where the vapour mass fraction

$$Y_m = \frac{X_m}{X_m(1 - M_g/M_d) + M_g/M_d} \tag{25}$$

of the droplet is given by the Clausius–Clapeyron's equation [4,8] with the droplet vapour mole fraction

$$X_m = \exp\left[\frac{h_v M_d}{\mathcal{R}}\left(\frac{1}{T_{bp}} - \frac{1}{T_p}\right)\right],$$

the droplet boiling point T_{bp}, the representative molecular weight M_d of the droplet and that of the gas phase, M_g. To account for the effect of the gas phase convection and the contribution of vapour concentration to the droplet heating process, modified Nusselt and Sherwood numbers are used. The expressions Nu, Sh, Sc and Pr [19] read

$$Sh = 2\left(1 + 0.3\frac{Re_p^{1/2} Sc_p^{1/3}}{F(B_M)}\right),$$

$$Nu = 2\frac{\ln(1 + B_T)}{B_T}\left(1 + \frac{0.3 Re_p^{1/2} Pr_p^{1/3}}{F(B_T)}\right),$$

$$Sc = \frac{\mu_g}{D_v \rho_g} \quad \text{and}$$

$$Pr = \frac{C_{pg}}{k_g},$$

respectively, where

$$F(B_{M,T}) = (1 + B_{M,T})^{0.7}\frac{\ln(1 + B_{M,T})}{B_{M,T}}.$$

The Spalding heat transfer number [19] is defined as

$$B_T = \frac{C_{pL}(T_g - T_s)}{L_{eff}} \tag{26}$$

with the specific heat capacity C_{pg} of the gas, the thermal conductivity k_g, the power Q_L spent on droplet heating and $L_{eff} = L + (Q_L/\dot{m}_p)$.

For validation of the vaporisation submodel, comparisons of the simulation results with the experimental zero gravity data by Nomura et al. [12] were performed. Therefore, suspended n-heptane droplets in a nitrogen atmosphere at 0.1 MPa at temperatures of 471 K, 555 K, 648 K and 741 K were considered. The initial n-heptane droplet radius was 0.3 mm.

Fig. 1 shows a comparison between the experimental data and the simulation results. One can observe a good agreement for the radius evolution of the evaporating n-heptane droplets for the various temperatures. The aim of presenting Fig. 1 is to

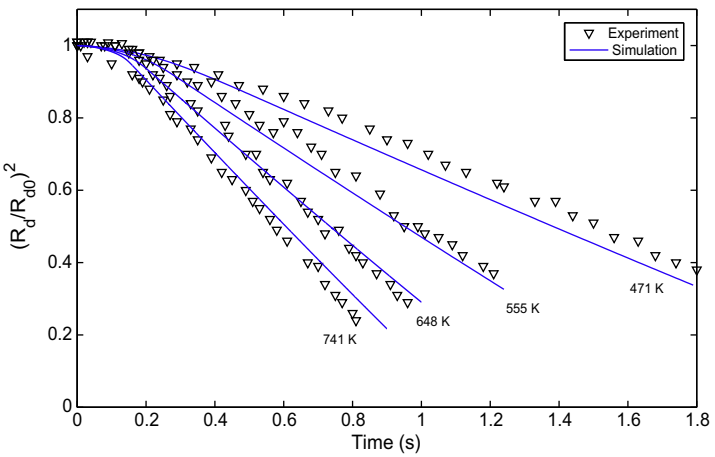

Fig. 1. The square of the ratio of droplet radius to its initial radius (R_d/R_{d0}^2) versus time as obtained by Nomura et al. [12] and the results obtained by calculations for evaporating n-heptane droplets at a pressure of 0.1 MPa and an initial gas temperatures of 471 K, 555 K, 648 K and 741 K.

validate the implementation of the evaporation model. With the study presented in Fig. 1, identification of a reasonable sub-model to describe evaporation of droplets within the new framework is intended.

3.4. Dispersed phase and continuous phase coupling

The expectations $\langle S_m^I \rangle$ and $\langle S_{U_i}^I \rangle$ are the source terms appearing in the Eqs. (2) and (3), respectively. $\langle S_m^I \rangle$ accounts for the mass transfer between droplet and gas phases due to evaporation and $\langle S_{U_i}^I \rangle$ accounts for the influence of the droplets on the mean gas phase momentum. $\langle S_m^I \rangle$ and $\langle S_{U_i}^I \rangle$ are computed from the ensemble of computational droplet particles using the expressions

$$\langle S_m^I(x,t) \rangle = -\langle R \rangle \left[\widetilde{\frac{1}{m_p} \frac{dm_p(t)}{dt}} \right]_p \tag{27}$$

and

$$\langle S_{U_i}^I(x,t) \rangle = \langle R \rangle \left[\widetilde{\left(\frac{U_{p,i} - U_{s,i}}{\tau_p} \right)}_p - \widetilde{\left(\frac{U_{p,i}}{m_p} \frac{dm_p}{dt} \right)}_p \right] \tag{28}$$

Moreover, the mass change $\Delta t \int\int\int_\Omega \langle S_m^I(\mathbf{x},t) \rangle d\mathbf{x}$ in cell Ω during a time step of size Δt is consistently added to the gas particles in that cell proportional to their weights.

4. Validation

In the implementation of the new modeling framework for statistically stationary evaporating two-phase flows, a hybrid particle/finite-volume algorithm as proposed by Jenny et al. [9] is used to compute the MDF of the continuous phase. The Reynolds averaged Navier–Stokes (RANS) equations are solved to obtain the mean velocity field, where the Reynold stresses plus mean energy source term are obtained from the particle solution. Therefore, the stochastic differential equations presented in Section 3 are solved.

The dispersed phase motion is consistently calculated by solving the additional MDF equation also presented in Section 3. Therefore, as shown by Minier and Peirano [20], equivalent computational particles are evolved. A short outline of the framework is shown in Fig. 2. This framework is capable of handling

- dispersed phase motion in the physical domain and evolution of its properties,
- dispersed phase particles of varying size,
- influence on mean mass and momentum of the continuous phase due to the evaporated dispersed phase, and
- influence on the momentum of the continuous phase due to dispersed phase momentum.

This framework has been used to predict the experimental results obtained by Sommerfeld and Qiu [13] for the evaporating iso-propyl alcohol spray. A good overall agreement is observed.

Naud [8] used a framework similar as the one presented here to model the effect of evaporating sprays. The results are encouraging, but the method lacks rigorous two-way coupling, i.e. the influence of the droplet motion on the gas velocity is ignored. Chen and Pereira [5] used a Lagrangian stochastic separated-flow (SSF) model for spray calculation. However, they did not account for the influence of the evaporated dispersed phase on the continuous phase momentum. Their model also lacks the effect of seen gas pressure gradient on the dispersed phase motion, which has minor influence in most cases, however.

4.1. Experimental configuration and the computational setup

For validation, the experiments performed by Sommerfeld et al. [13] are employed. This experiment has been widely used to validate turbulent evaporating spray simulations [6–8]. A sketch of the experimental configuration [13] is presented in Fig. 3.

For the single phase flow measurements, the air flow was seeded with small spherical glass beads approximately 3 μm in diameter. For the two-phase flow measurements, iso-propyl alcohol liquid at ambient temperature was injected into the cylinder having an inner diameter of 0.2 m and a length of 1.5 m. The liquid is injected through a nozzle of 0.02 m diameter located at the center of the cylindrical configuration. A coflowing air stream at 100 °C enters the domain through an annulus having an outer diameter of 64 mm. Detailed experimental measurements for both single- and two-phase flows are available for the axial locations X = 3, 25, 50, 100, 200, 300 and 400 mm in the downstream direction. Comparisons between the experimental data and the simulation results for single- and two-phase flows are discussed in Sections (4.2) and (4.3).

From the experimental measurements, it can be ascertained that the spray is approximately axisymmetric. For the computations, we chose a domain ranging from 0 m to 0.6 m in the axial direction and from 0 m to 0.097 m in the radial direction.

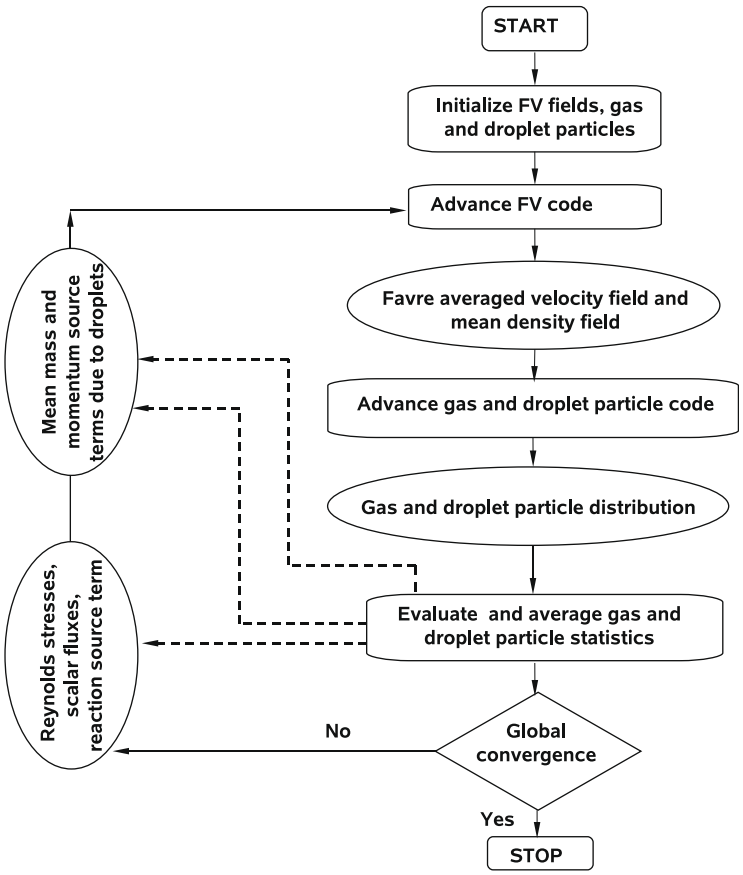

Fig. 2. Flow chart of the proposed framework.

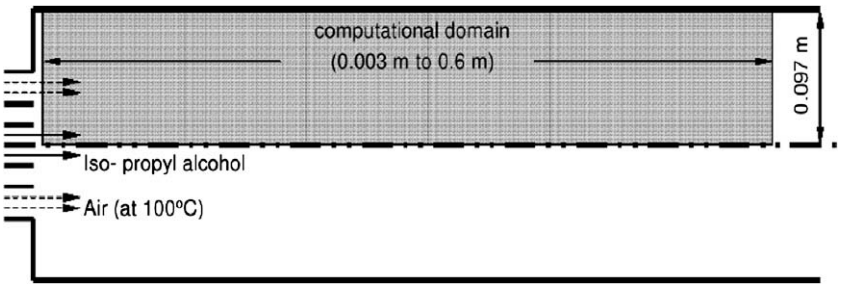

Fig. 3. Schematic representation of the experimental setup used by Sommerfeld et al. [13].

4.2. Results for the single phase flow

Previous studies [4,6–8] show that the drag term in Eq. (16) is dominant, thus signifying the importance of correct predictions of the single phase flow field. Therefore, in a first validation study single phase flow was considered [13].

For the computations, a 90×50 grid was used, which has been refined near the nozzle to resolve the recirculation zone. Moreover, an average of 30 computational gas particles per grid cell were employed. At the inlet, Dirichlet boundary conditions based on the experimental flow profiles at the axial position $X = 3$ mm were applied and at the walls and at the symmetry axis, slip boundary conditions were employed.

Calculated mean and rms gas velocity components are shown in Figs. 4–7 together with the experimental data [13] and the simulation results obtained by Naud [8]. Overall, a reasonable agreement can be observed. Part of the disagreement of both the axial and radial rms velocity components near the nozzle region can be attributed to the fact that some of the required information at the inflow boundary is not available and had to be estimated. Similar observations were made by Naud

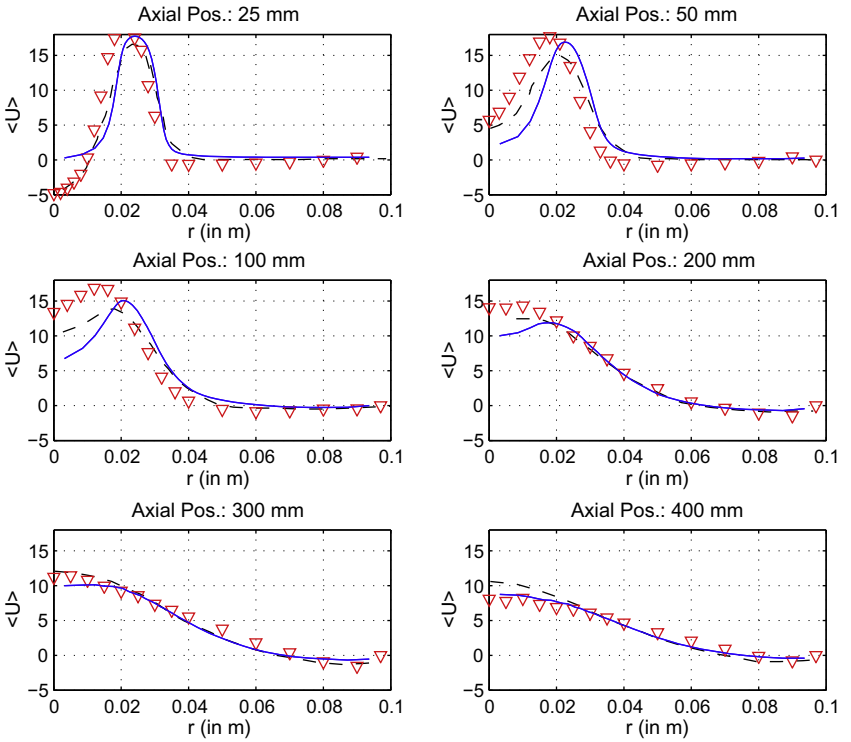

Fig. 4. Mean axial gas velocity component. The continuous line, dashed line, and ▽ represent the radial profiles obtained from the present simulation, Naud [8] and experiment [13], respectively.

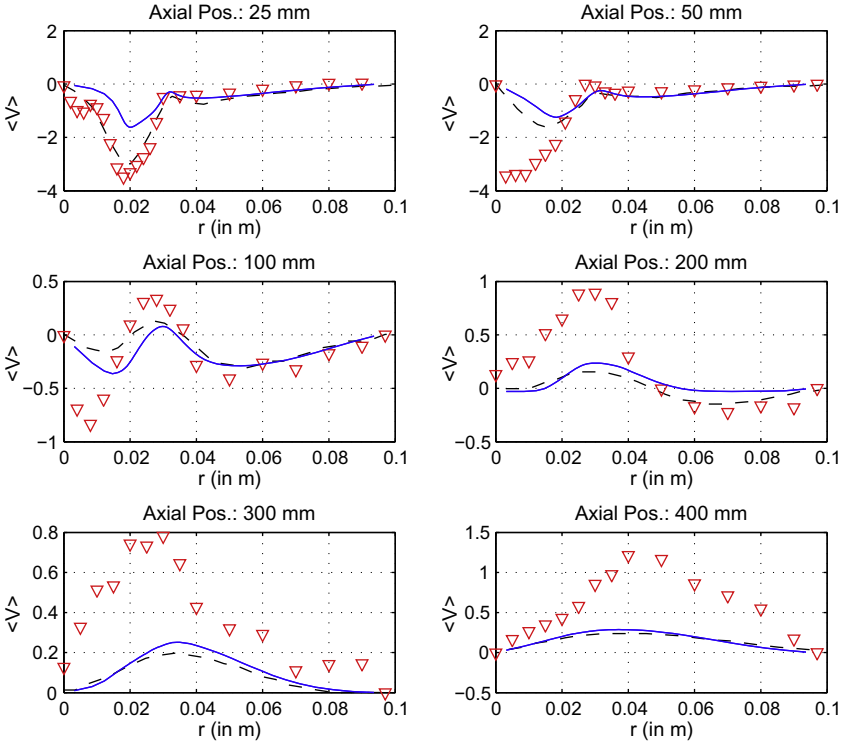

Fig. 5. Mean radial gas velocity component. The continuous line, dashed line, and ▽ represent the radial profiles obtained from the present simulation, Naud [8] and experiment [13], respectively.

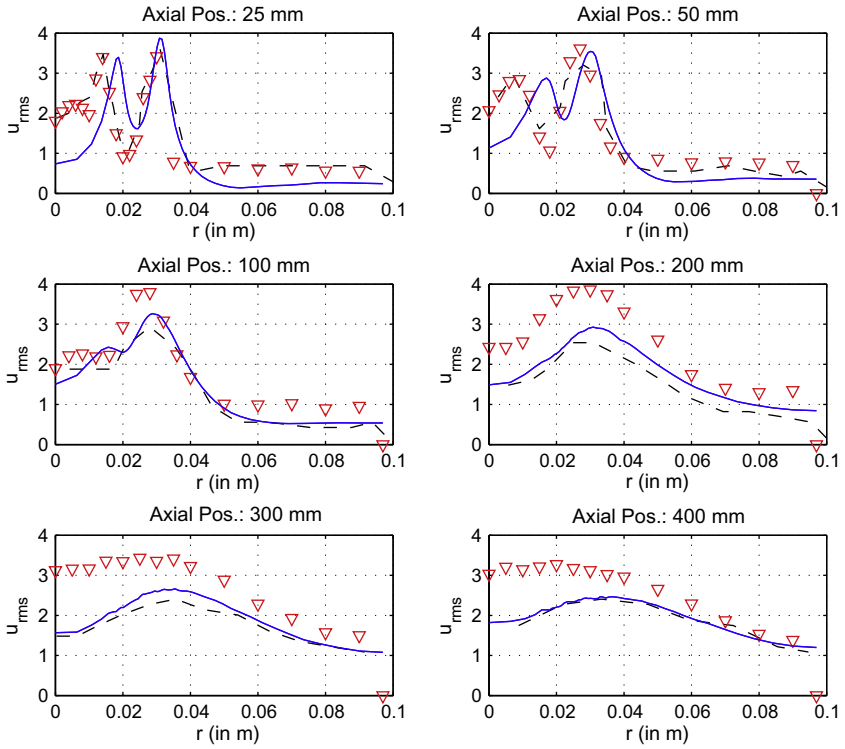

Fig. 6. Rms of the axial gas velocity component. The continuous line, dashed line, and ▽ represent the radial profiles obtained from the present simulation, Naud [8] and experiment [13], respectively.

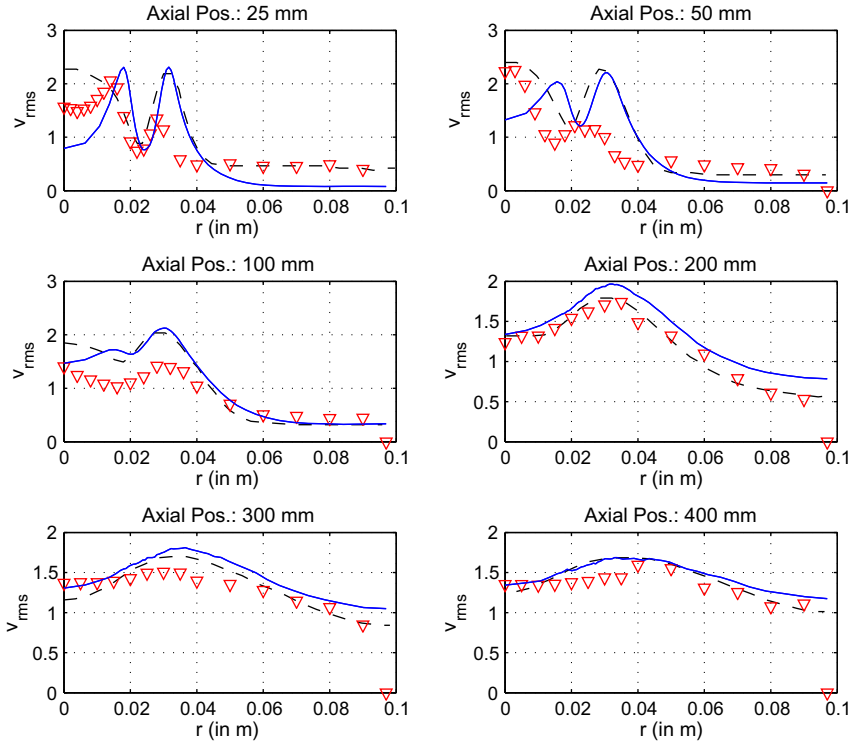

Fig. 7. Rms of the radial gas velocity component. The continuous line, dashed line, and ▽ represent the profiles obtained from the present simulation, Naud [8] and experiment [13], respectively.

[8] in his study. The improved gas flow profiles obtained by Naud [8] at section $X = 25$ mm in Figs. 4–7 might be due to the choice of better inlet boundary conditions.

4.3. Results for the dispersed phase flow

For the dispersed phase flow, note that convection plays a major role in evaporation and dominates the process, if the droplets spend a long time within the domain. Therefore, a correct prediction of droplet motion is crucial for a good evaporation rate prediction. On the other hand, the evaporation process affects the droplet motion as small-sized droplets tend to

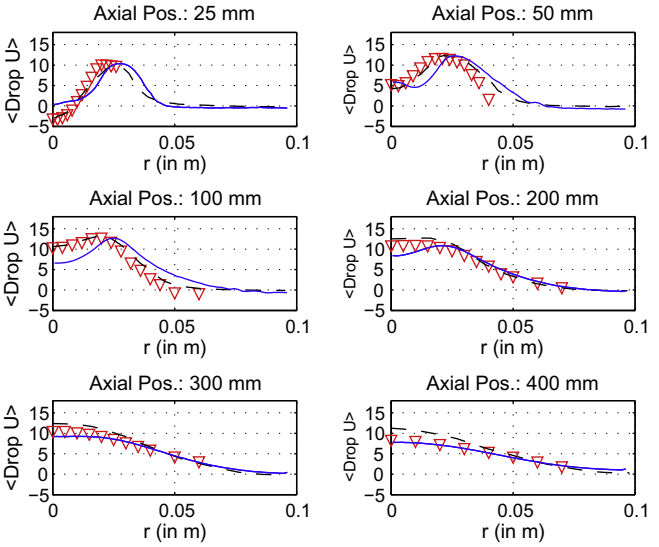

Fig. 8. Mean axial droplet velocity component. The continuous line, dashed line, and ▽ represent the radial profiles obtained from the present simulation, Naud [8] and experiment [13], respectively.

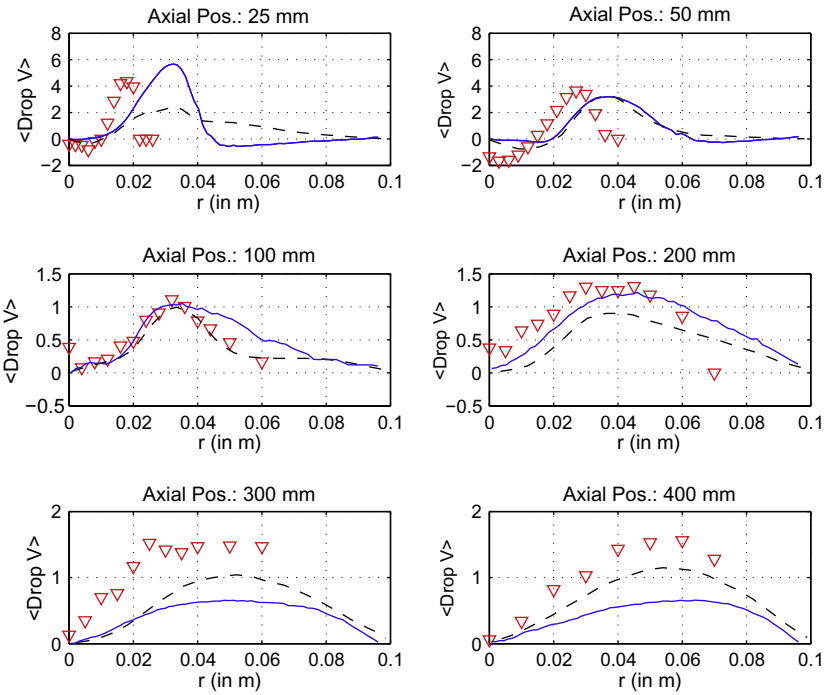

Fig. 9. Mean radial droplet velocity component. The continuous line, dashed line, and ▽ represent the radial profiles obtained from the present simulation, Naud [8] and experiment [13], respectively.

drift faster towards the instantaneous gas velocity [6]. Here, a grid with 100×70 cells in the axial and radial directions, which is refined near the nozzle region, was used for the computations. Again, an average of 30 computational gas particles and 30 computational droplet particles per cell were employed. Note that these particle numbers are much smaller than those used in previous studies, which is due to the hybrid FV/particle method [9,14], the employed time-averaging scheme [9], and local particle time-stepping [10]. Computational cost analysis associated with the present study are presented later in Section 4.4.4.

As in the single phase flow study, Dirichlet boundary conditions based on the flow profiles at section $X = 3$ mm were applied at the inlet and a droplet-size distribution consistent with the published experimental data [13] was imposed.

A quantitative comparison of the simulation results with the experimental data [13] and the simulation results of Naud [8] is shown in the Figs. 8–13. The overall agreement is reasonable. Figs. 8 and 9 show the mean radial droplet velocity profiles at the axial locations $X = 25$, 50, 200, 300 and 400 mm. A reasonable agreement of the mean axial velocity component

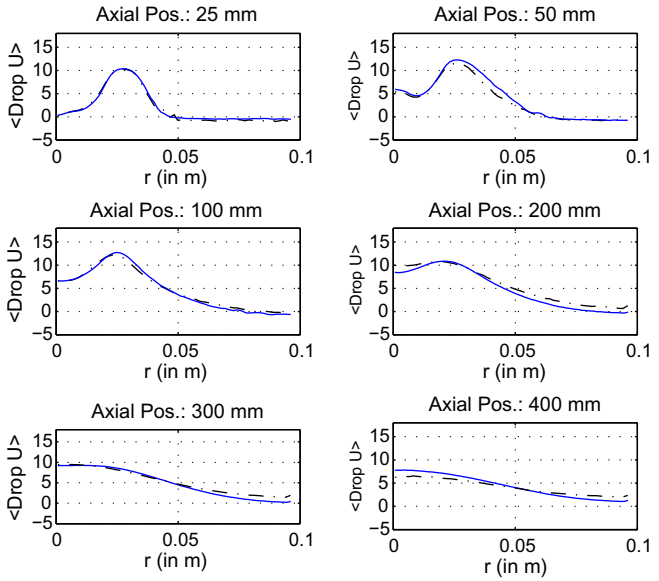

Fig. 10. Mean of the axial droplet velocity component. The continuous line and dash-dot line represent the radial profiles obtained from the present simulation with and without the influence of droplets on the mean gas momentum, respectively.

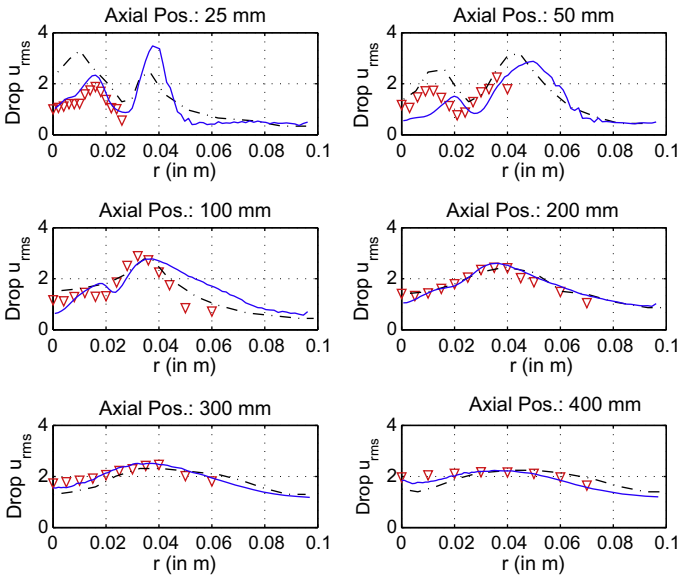

Fig. 11. Rms of the axial droplet velocity component. The continuous line, dashed line, and ▽ represent the radial profiles obtained from the present simulation, Naud [8] and experiment [13], respectively.

with the experimental data can be observed, but along the centreline, near the valve region, it is underpredicted. Again, this deviation can be attributed to the lack of sufficient experimental inflow data, which is a known concern in spray simulations.

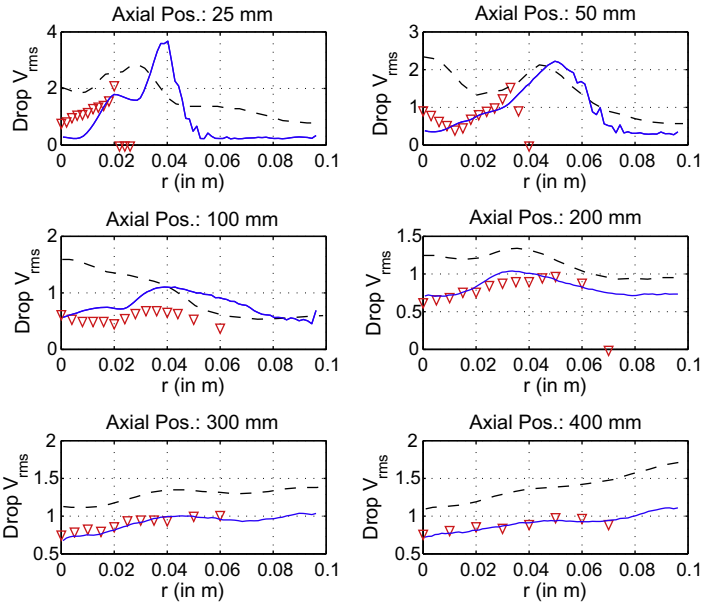

Fig. 12. Rms of the radial droplet velocity component. The continuous line, dashed line, and ▽ show represent the radial profiles obtained from the present simulation, Naud [8] and experiment [13], respectively.

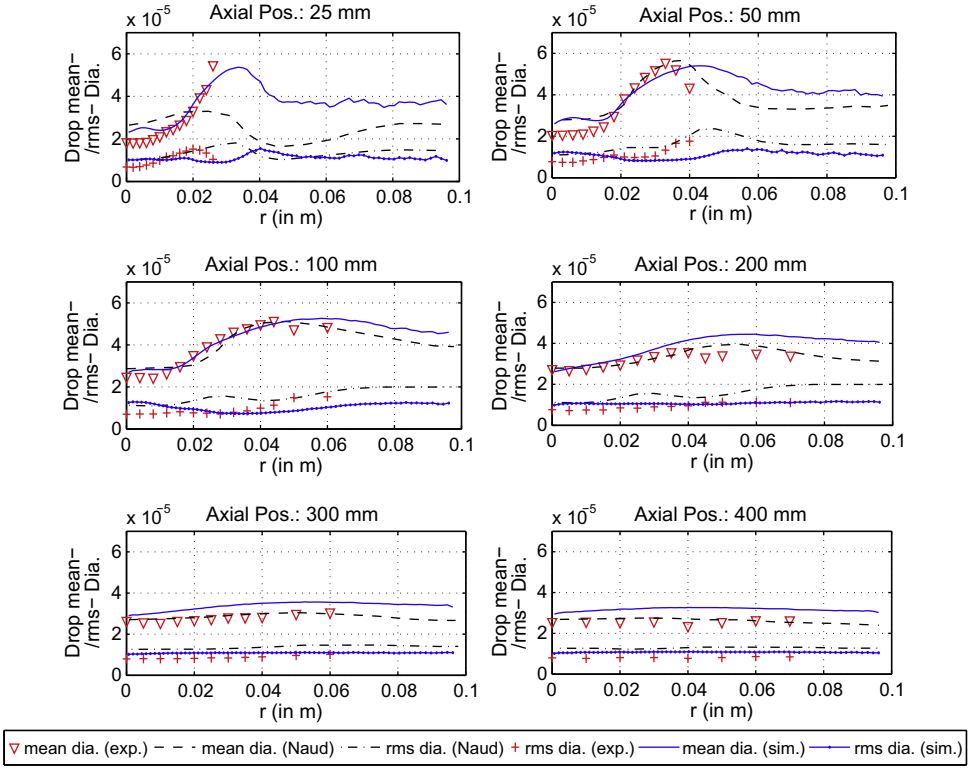

Fig. 13. Mean and rms droplet diameters. The continuous line, dashed line and ▽ s how the mean radial profiles obtained from the present simulation, Naud [8] and experiment [13] respectively. The symboled-continuous line, dash-dot line and the symbol '+' represent the droplet rms radial profiles obtained from the present simulation, Naud [8] and experiment [13], respectively.

Table 2
Test locations in the domain.

Location	Distance in x-direction (m)	Distance in y-direction (m)
1	0.1	0.06
2	0.2	0.04
3	0.4	0.02

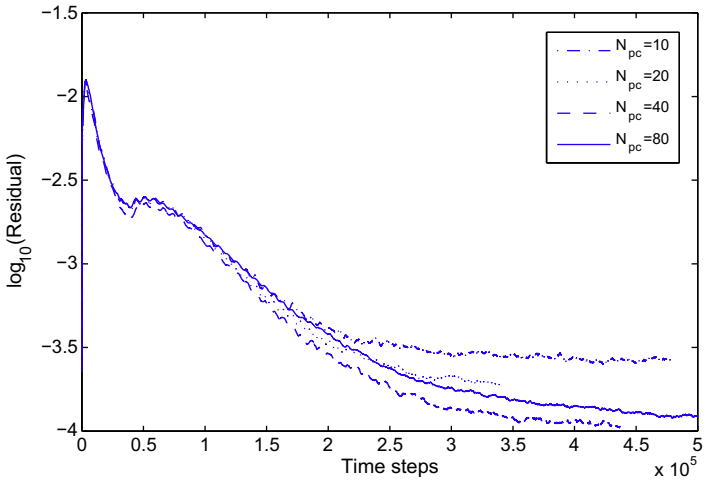

Fig. 14. Convergence histories: Logrithm of the residuals in the finite-volume code for 70×50 grid with N_{pc} ranging from 10 to 80 particles per grid cell each of gas and droplet phase against time steps.

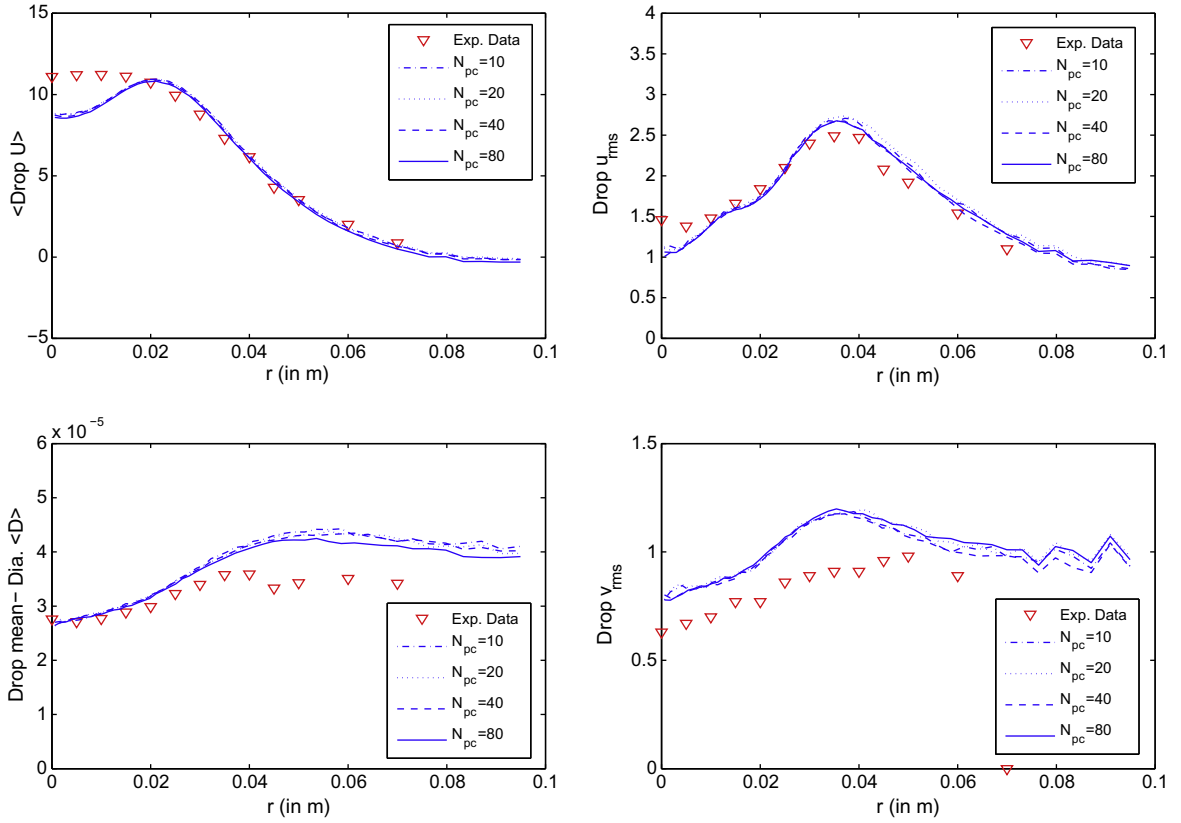

Fig. 15. Radial profiles of mean axial droplet velocity (top left), rms axial droplet velocity (top right), mean droplet diameter (bottom left) and rms radial droplet velocity (bottom right) at axial location $X = 0.2$ m computed on 70×50 grid with N_{pc} ranging from 10 to 80 particles per grid cell each of gas and droplet phase.

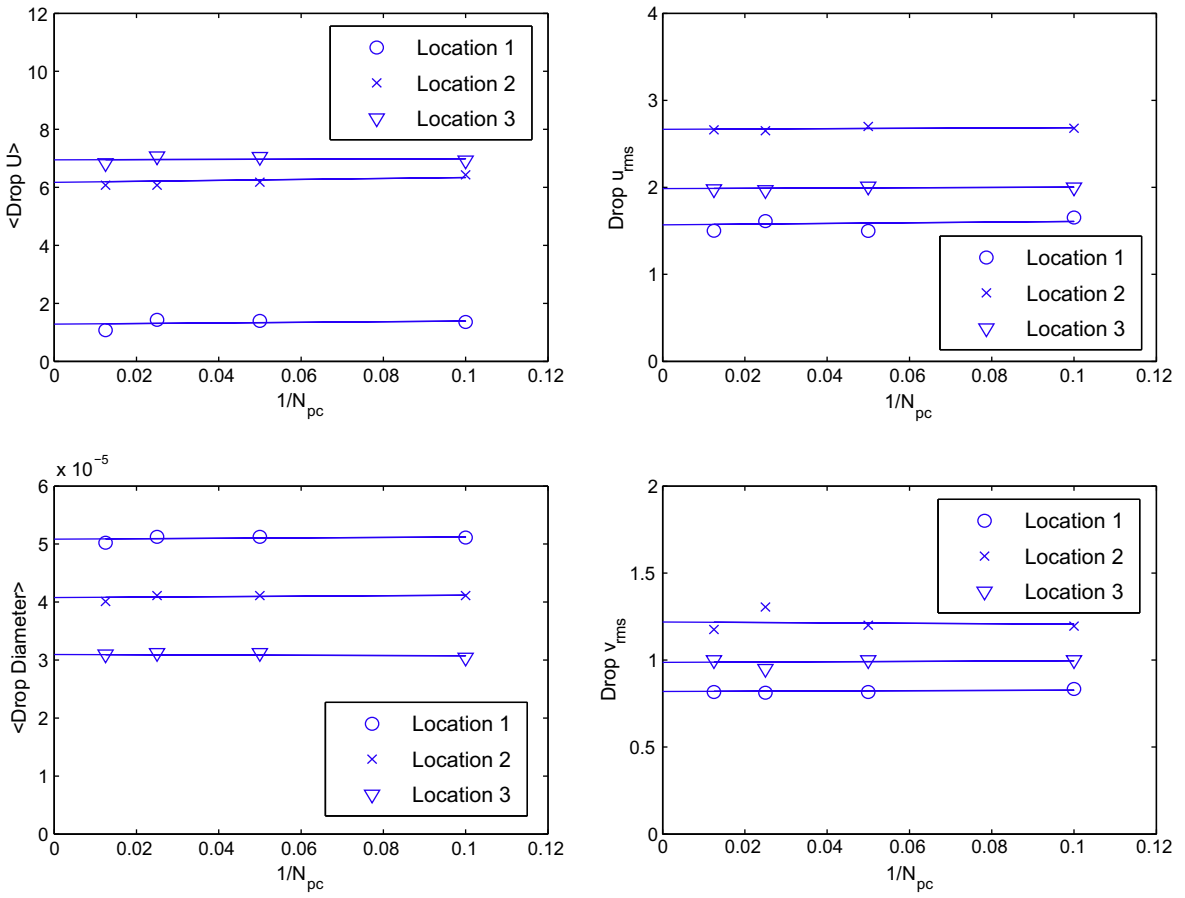

Fig. 16. Bias convergence studies: Droplet properties against N_{pc}^{-1} at different locations (Table 2) showing the bias error for $K = 10{,}000$.

Due to the presence of the droplets, the mean gas momentum is modified which in turn modifies the droplet momentum through the drag term. Naud [8] did not consider the influence of droplets on the mean gas momentum. However, from Fig. 10 it is ascertained that ignoring the influence of the droplets on the mean gas momentum produces no significant alteration in the prediction of the mean velocity profiles in the present case study. Thus confirming the validation of Naud's assumption [8].

Figs. 11 and 12 shows the radial rms droplet velocity profiles and it can be observed that the present calculations are in very good agreement with the experimental data [13]. A significant improvement (both qualitative and quantitative) in prediction of rms radial droplet velocity over the results obtained by Naud [8] is observed.

Finally, Fig. 13 shows the mean and rms droplet diameters obtained from the present simulation together with the experimental data [13] and the results by Naud [8]. Again, a good quantitative agreement with the experimental data can be observed.

4.4. Convergence study

In this section, results obtained from numerical experiments are used to study the bias and spatial discretization errors. For convenience, locations 1–3 as defined in Table 2 are chosen to quantify bias and spatial discretization errors.

4.4.1. Stationary solution

The hybrid algorithm for the two-phase flow is designed to handle statistically stationary flows. Fig. 14 shows the decay of the residual (2-norm of energy change per finite-volume time step) as a function of time steps for varying numbers of both gas and droplet particles per cell (N_{pc}) ranging from 10 to 80. Calculations are performed on a 70×50 grid with a time-averaging factor K of 10000. It can be observed that the residuals gradually decrease.

4.4.2. Bias error

Bias error is a deterministic error occurring due to usage of a finite number of particles. In the present section, the aim is to study the influence of different values of time-averaging factors K and varying numbers of both gas and droplet particles

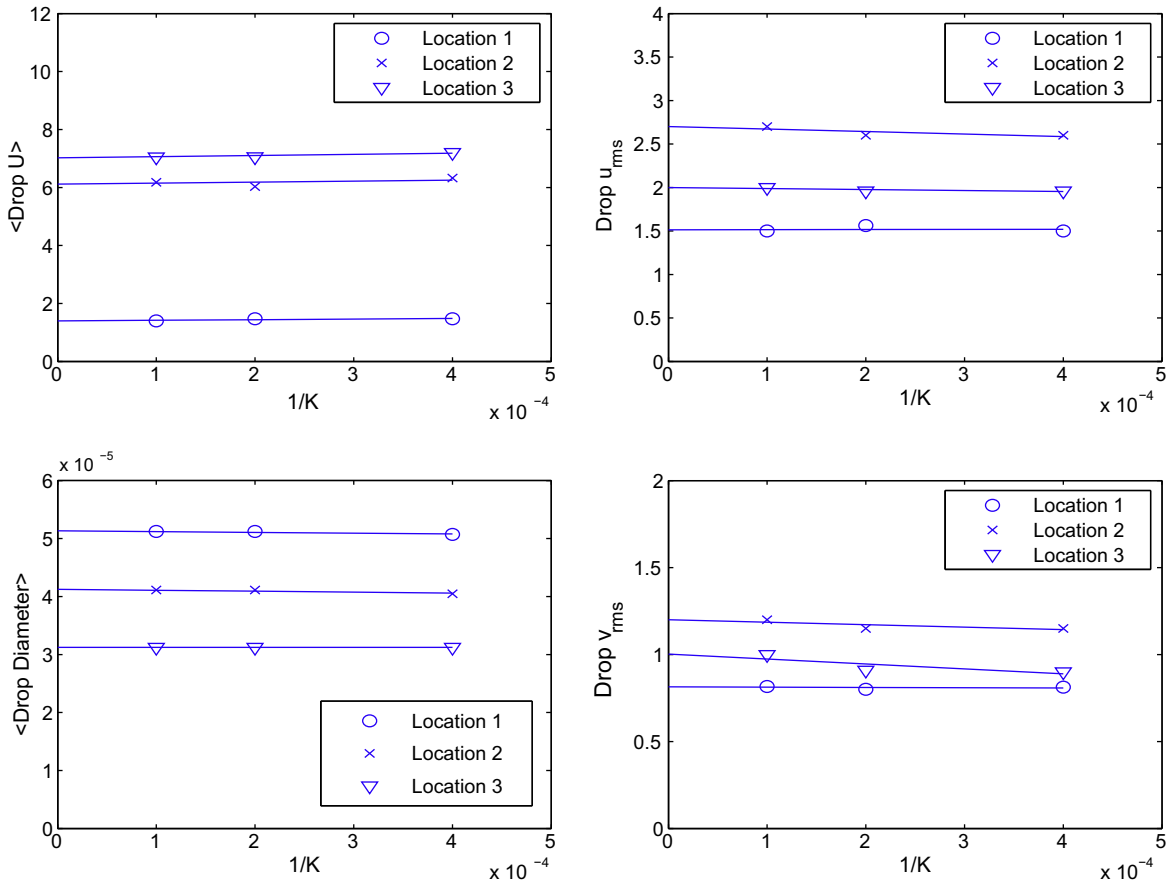

Fig. 17. Bias convergence studies: Droplet properties against inverse of time-averaging factor K at different locations (Table 2) showing the bias error for $N_{pc} = 20$.

per cell. For this purpose, calculations were performed on a grid with 70×50 cells. For a given number of both gas and droplet particles per cell ($N_{pc} = 20$, i.e. 20 gas and 20 droplet particles per cell), calculations are performed for different values of time-averaging factors. Similarly, for $K = 10{,}000$, numerical experiments are performed for varying numbers of both gas and droplet particles per cell ranging from 10 to 80. Fig. 15 shows the radial profiles of various droplet properties at $X = 0.2$ m for varying numbers of both gas and droplet particles per cell for $K = 10000$. The small variations between the radial profiles imply that the bias error is small.

To quantify the bias error, mean axial droplet velocity, rms axial droplet velocity, mean droplet diameter and rms radial droplet velocity obtained from calculations at various locations (Table 2) are plotted against N_{pc}^{-1} in Fig. 16. Symbols are the numerical data and solid lines are the linear least-square fits obtained from the numerical data. The slopes of these lines indicate the magnitude of the bias error. In Fig. 16, it can be noticed that the slopes are small thus indicating very small bias error.

Fig. 17 shows the plots of various droplet properties against K^{-1} at various locations (Table 2) for a given number of both gas and droplet particles $N_{pc} = 20$. Symbols represent the numerical data, solid lines are the linear least-square fits obtained from the numerical data and again their slopes indicate the magnitude of bias error. From the plots it can be ascertained that the bias error is very small for the mean axial droplet velocity and mean droplet diameter. For rms droplet velocities, the bias error gets larger for time-averaging factors $K \leqslant 2500$. Thus, it can be safely concluded that time-averaging with $K > 5000$ and $N_{pc} = 20$ leads to results, which are essentially free of any bias error.

4.4.3. Spatial discretization error

Spatial discretization errors are deterministic errors occurring due to the usage of finite number of grid cells. To quantify the spatial discretization error, calculations were performed on $40 \times 30, 70 \times 50, 100 \times 70$ and 130×90 grids for $K = 10{,}000$ and $N_{pc} = 20$ (20 gas and 20 droplet particles per cell). The same droplet statistics at the locations of Table 2 was considered as for the bias error studies. Fig. 18 shows the plots of mean axial droplet velocity, rms axial droplet velocity, mean droplet diameter and rms radial droplet velocity against $M_x^{-1}M_y^{-1}$. Symbols represent the numerical results and solid lines are the linear least-square fits to the numerical data. From the figure, it can be deduced that the spatial discretization is worse

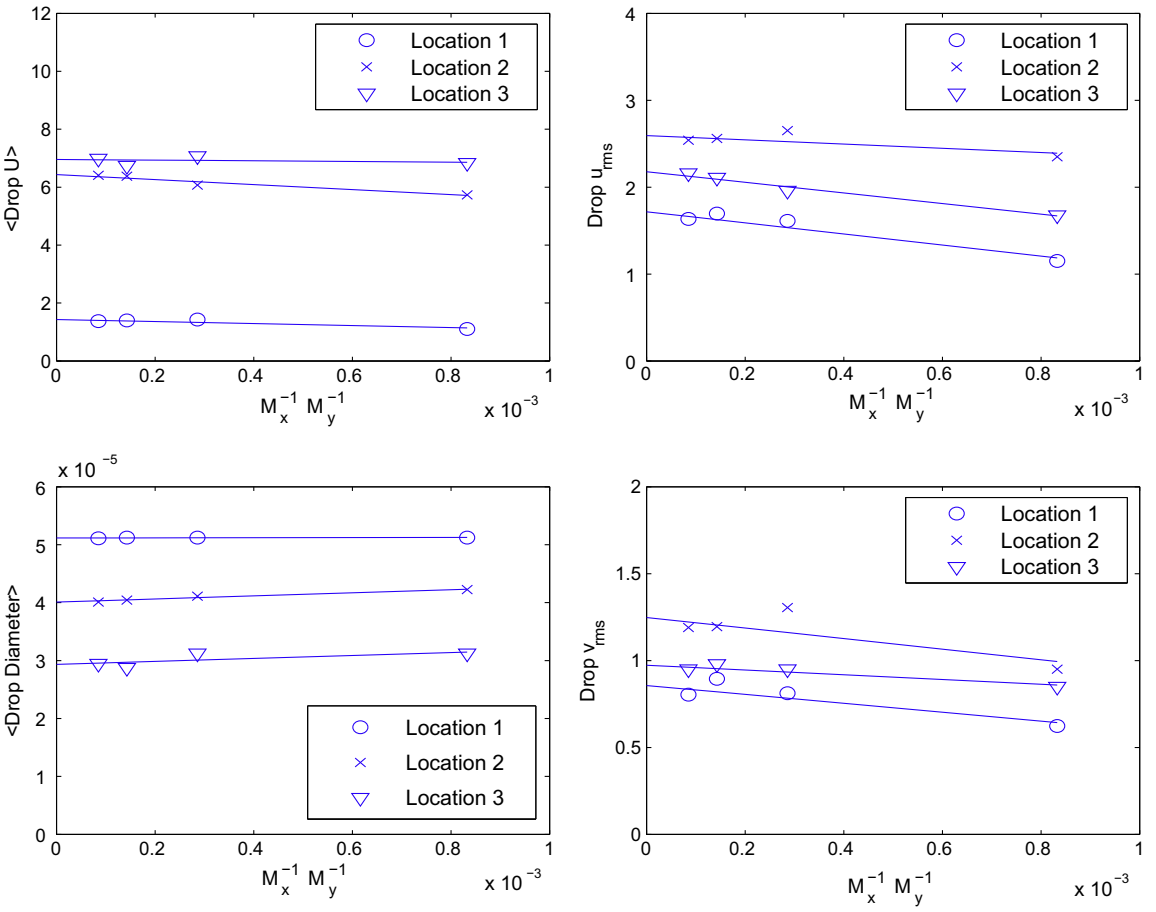

Fig. 18. Grid convergence studies: Droplet properties against $M_x^{-1}M_y^{-1}$ at different locations (Table 2) showing the bias error for $N_{pc} = 20$.

Table 3
Simulations for computational cost assessment; $M_xM_y = 70 \times 50$, number of timesteps $N_{timesteps} = 100$.

Simulation	N_{pc}	T_{CPU} (s)	n_{conv} (approx.)
A	20	50.16	300,000
B	40	97.06	300,000
C	80	188.37	300,000

Table 4
Coefficients determined from simulations A, B and C.

ΔN_{pc}	ΔT_{CPU}	$c_{particle}$	$c_{overhead}$
$N_{pc}^B - N_{pc}^A = 20$	$T_{CPU}^B - T_{CPU}^A = 46.9$ s	3.3499×10^{-6} s	9.3147×10^{-6} s
$N_{pc}^C - N_{pc}^B = 40$	$T_{CPU}^C - T_{CPU}^B = 91.31$ s	3.2611×10^{-6} s	7.8570×10^{-6} s
$N_{pc}^C - N_{pc}^A = 60$	$T_{CPU}^C - T_{CPU}^A = 138.21$ s	3.2907×10^{-6} s	1.1685×10^{-5} s

for the rms than for the mean droplet quantities. However for both axial and radial rms droplet velocity components, a grid which is finer than 70×50 ($M_x^{-1}M_y^{-1} = 2.85 \times 10^{-4}$) is required to significantly reduce the spatial discretization error at these locations.

4.4.4. Computational cost

The computational cost [21] associated with such a particle PDF solution algorithm can be expressed as

$$T_{total} \approx n_{conv} M_x M_y (c_{particle}(2\ N_{pc}) + c_{overhead}), \tag{29}$$

where T_{total} is the total CPU time, $c_{particle}$ the CPU time per particle per time step, $c_{overhead}$ the CPU time per time step for non-particle computations, M_x the number of cells in x-direction, M_y the number of cells in y-direction, 2 N_{pc} the number of both gas and droplet particles per cell and n_{conv} the number of time steps required to reach a statistically stationary solution.

In the present study, computational cost analysis was performed on a 70×50 grid. The CPU times T^{A}_{CPU}, T^{B}_{CPU} and T^{C}_{CPU} per 100 time steps were measured for $N_{pc} = 29, N_{pc} = 40$ and $N_{pc} = 80$, respectively. Table 3 shows T_{CPU} and n_{conv} measured for the simulations A, B and C. The parameters $c_{particle}$ and $c_{overhead}$ are given as

$$c_{particle} = \frac{\Delta T_{CPU}}{N_{timesteps}\ M_x\ M_y\ (2\Delta N_{pc})} \tag{30}$$

and

$$c_{overhead} = \frac{T_{total}}{N_{timesteps}\ M_x\ M_y} - c_{particle}(2\ N_{pc}), \tag{31}$$

where $N_{timesteps} = 100$ is the number of time steps considered. ΔT_{CPU} the difference between the measured CPU times for different numbers of particles per cell and 2 ΔN_{pc} the difference in the number of particles per cell. Table 4 shows the coefficients determined from simulations A, B and C. Computations were performed on a 2.2 GHz Intel machine. From the table, it can be ascertained that there is very small variation in the computational cost per particle per cell for the cases considered. Thus, it can be concluded that the computational cost increases linearly with increasing number of particles per cell, i.e. the usage of significantly fewer particles leads to significant computational savings.

5. Conclusions

The aim of the present study was to devise a framework for spray combustion modeling, where the influence of the droplet motion on the mean gas momentum is significant. Therefore, a unified PDF modeling framework and a new hybrid solution algorithm to simulate turbulent evaporating sprays was developed. Two-way coupling between the droplet and gas phases is implemented and an infinite thermal conductivity (ITC) evaporation sub-model is used. Opposed to previous approaches, the decorrelation between droplet and seen gas velocities is formulated based on individual separation and correlation length scales. To enhance the computational efficiency, a local particle time-stepping algorithm [10] was implemented and a particle time-averaging technique [9] is employed to reduce statistical and bias errors. This enables the use of much fewer computational gas and droplet particles per grid cell in comparison to previous studies [5,8].

The PDF algorithm was validated with the experimental data of a turbulent evaporating iso-propyl alcohol spray [13]. Overall, reasonable agreement can be observed.

References

[1] E. Loth, Numerical approaches for motion of dispersed particles, droplets and bubbles, Prog. Energy Combust. Sci. 26 (2000) 161–223.
[2] R.H. Rangel, Heat transfer in vortically enhanced mixing of vaporizing droplet sprays, Annu. Rev. Heat Transfer 4 (1992) 331.
[3] G. Gouesbet, A. Berlemont, Eulerian and Lagrangian approaches for predicting the behaviour of discrete particles in turbulent flows, Prog. Energy Combust. Sci. 25 (1999) 133–159.
[4] X.Q. Chen, J.C.F. Pereira, On the influence of gas temperature on spray evaporation, in: Proceedings of the International Symposium on Turbulence, Heat and Mass Transfer, Lisbon Portugal, 1994, pp. 10.2.1–10.2.7.
[5] X.Q. Chen, J.C.F. Pereira, Prediction of evaporating spray in anisotropically turbulent gas flow, Numer. Heat Transfer, Part A 27 (1995) 143–162.
[6] X.Q. Chen, J.C.F. Pereira, Computation of turbulent evaporating sprays: with well-specified measurements: a sensitivity study on droplet properties, Int. J. Heat Mass Transfer 39 (1996) 441–454.
[7] M. Sommerfeld, H.H. Qiu, Analysis of isothermal and evaporating turbulent sprays by phase-doppler anemometry and numerical calculations, Int. J. Heat Fluid Flow 19 (1998) 10–22.
[8] B. Naud, PDF modeling of turbulent sprays and flames using a particle stochastic approach. Ph.D. Thesis, Delft University of Technology, 2003.
[9] P. Jenny, S.B. Pope, M. Muradoglu, D.A. Caughey, A hybrid algorithm for the joint pdf equation of turbulent reactive flows, J. Comput. Phys. 166 (2) (2001) 218–252.
[10] M. Muradoglu, S.B. Pope, Local time-stepping algorithm for solving the probability density function turbulence model equations, AIAA J. 40 (2002) 1755–1763.
[11] S.S. Sazhin, T. Kristyadi, W.A. Abdelghaffar, M.R. Heikal, Models for fuel droplet heating and evaporation: comparative analysis, Fuel 85 (2006) 1613–1630.
[12] H. Nomura, Y. Ujiie, H.J. Rath, J. Sato, M. Kono. Experimental study on high-pressure droplet evaporation using microgravity conditions, in: Proceedings of the Combustion Institute, 1996, pp. 1267–1273.
[13] M. Sommerfeld, H.H. Qiu, Experimental studies of spray evaporation in turbulent flow, Int. J. Heat Fluid Flow 19 (1998) 10–22.
[14] M. Muradoglu, S.B. Pope, D.A. Caughey, The hybrid method for the pdf equations of turbulent reactive flows: consistency conditions and correction algorithms, J. Comput. Phys. 172 (2001) 841–878.
[15] B. Rembold, P. Jenny, A multiblock joint pdf finite-volume hybrid algorithm for the computation of turbulent flows in complex geometries, J. Comput. Phys. 220 (2006) 59–87.
[16] R.S. Miller, K. Harstad, J. Bellan, Evaluation of equilibrium and non-equilibrium evaporation models for many-droplet gas–liquid flow simulations, Int. J. Multiphase Flow 24 (1998) 1025–1055.
[17] A. Berlemont, M.S. Grancher, G. Gouesbet, On the lagrangian simulation of turbulence on droplet evaporation, Int. J. Heat Mass Transfer 34 (1991) 2805–2812.

[18] D.B. Spalding, The combustion of liquid fuels, in: Proceedings of the Combustion Institute, 1953, pp. 847–864.
[19] W.A. Sirignano, Fluid Dynamics and Transport of Droplets and Sprays, Cambridge University Press, Cambridge, 1999.
[20] J.P. Minier, E. Peirano, The pdf approach to turbulent polydispersed two-phase flows, Phys. Rep. 352 (2001) 1–213.
[21] P. Jenny, S.B. Pope, M. Muradoglu, D.A. Caughey, PDF simulations of a bluff-body stabilized flow, J. Comput. Phys. 169 (2001) 1–23.